

# Fully coupled aero-thermo-elastic analysis of shock-wave and turbulent boundary layer interactions

Al Shahriar\*, and Kourosh Shoele<sup>†</sup> *FAMU-FSU College of Engineering, Tallahassee, FL, 32304* 

Fully coupled aero-thermo-elastic simulations have been conducted to investigate fluid-thermal-structural interaction in shockwave turbulent boundary layer interaction. A finite element thermoelastic structural solver and the finite difference flow solver are coupled together and run simultaneously to capture the underlying physics and aero-thermo-elastic effects of the shockwave turbulent boundary layer interaction. A brief study on the laminar boundary shows the transition to turbulence due to the impact of the shockwave. The van Driest velocity profile, turbulent intensities, and Reynolds shear stress of the boundary layer have been evaluated to quantify the combined impact of panel flexibility and thermal dependency on the interactions. The thermal dependency of the panel material has a significant spatio-temporal impact on the interaction. Proper orthogonal decomposition is used to identify the dominant mode shapes of the panel oscillation that govern the interactions.

#### I. Introduction

High-speed supersonic and hypersonic flows are often characterized by shock wave boundary layer interactions (SBLI) and the complex nature of SBLI makes this topic an active area of research for more than seven decades and still offers open questions. SBLI poses many difficulties to high-speed vehicles and turbomachinery, more specifically airfoils operating at high speeds, control surfaces during supersonic/hypersonic flight, rocket nozzles, and high-speed engine inlets [1–5]. In 2001, David S. Dolling provided a comprehensive review of state-of-the-art research while discussing the most essential aspects of SBLI, many solved and unsolved problems of SBLI by that time, and provided useful suggestions to deal with the existing problems [5]. SBLI has several complex flow response modes including low-frequency oscillations, separation bubbles, peak heating, etc. [6]. There is extensive research that characterizes the role of SBLI over rigid structures using numerical and experimental approaches. Previous numerical and experimental investigations were conducted for laminar [7–12], turbulent [4, 13–20], and transitional [21, 22] boundary layers interactions. The numerical studies have utilized techniques such as large eddy simulation (LES) [16, 23–26] and direct numerical simulation (DNS) [20, 27, 28].

The dynamics of the boundary layer in high-speed flows are significantly influenced by the presence of a compliant interface. The aeroelastic behavior in such conditions is typically investigated using the canonical problem of panel flutter [29–31]. Panel flutter is a well-documented phenomenon where the boundary layer interacts with the flexible surface and due to the action of the pressure fluctuations as well as the inherent dynamic behavior of the coupled system, the panel starts to oscillate. Ostoich et al.[29] observed that the unstable eigenmodes of the initial laminar boundary layer which is usually of low amplitude, strengthen in time due to the panel motion. They also noticed a wave-like deflection of the panel which causes oscillating shocks.

The role of flexible structure in SBLI can be traced back in several research studies [32–35]. The first notable work of the interaction of an oblique shock with the flexible body can be found in [32]. For inviscid flow, it was observed that if the strength of the shock is increased, the amplitude and frequency of the limit-cycle (at least one other trajectory spirals into the original trajectory) oscillations will also increase for a constant incoming dynamic pressure. It was also found that the unsteadiness behavior created by the fluttering panel propagates along the expansion fan, reattachment, and reflected shock. Later Visbal extended his work for viscous flow where a Navier–Stokes solver linked with the nonlinear von Karman plate equations [33]. A non-periodic self-excited oscillation associated with the flexible structure was observed. He suggested that, because of such oscillation, an aeroelastic panel can be designed for passive flow control. According to Willems et al. [34], the motion of the panel plays a crucial role in influencing how incoming shocks are reflected and in shaping the characteristics of the separation bubble. When the surface of the panel undergoes increased deformation, it experiences both tensile and bending forces. These forces, in turn, excite the normal modes

<sup>\*</sup>Research Assistant, Mechanical Engineering, 2525 Postsdammer street, and AIAA Student member

<sup>&</sup>lt;sup>†</sup>Associate Professor, Mechanical Engineering, 2525 Postsdammer street

of the panel, leading to dynamic deflections in its motion. Specifically, the panel exhibits a notable static deflection that scales with the applied pressure, alongside minor vibrations that accompany this motion. Brouwer et al. [36] observed that the unsteady deformation brings trivial changes to the length and size of the separation bubble. But, static surface deformation can increase and decrease the bubble length significantly. They proposed that the surface curvature and surface velocity directly trigger the separation. Shinde et al. [22] observed a smaller separation bubble for the flexible panel. Compared with the rigid wall pressures, the mean wall pressure was smaller for the elastic panel near the separation and higher near the reattachment region. The skin friction coefficient is higher in the downstream region, where the bubble breaks with the spectral energy into small turbulent flow structures. The spectral energy is mostly localized near the reattachment region. Panel oscillations induce compression and expansion waves in the flow, while at the same time amplifying separation-shock dynamics for a two-way coupling of SBLI with flexible body [37]. Understanding the interplay between thermal coupling and fluid-structure interaction (FSI) is exceptionally challenging due to the complex and diverse range of scales involved. This complexity encompasses fluid and solid instabilities, as well as thermal transport dynamics. A critical aspect of this interaction is the relationship between the dominant timescale of the flexible surface and the low-frequency oscillation of the separation bubble. When these timescales align, temperature variations within the panel can profoundly affect the nonlinear dynamics between the structure and the fluid, potentially leading to significant changes in behavior and performance. Freydin et al. [38] investigated the aeroelastic response of a plate under turbulent shock wave boundary layer interactions (SBLI), analyzing experimental pressure fields to model fluid-structure responses, noting the significant role of boundary layer thickness in excitation processes. In a related study on flexible panels, Gao et al. [39] observed increased pressure variation amplitudes and altered separation zone configurations, suggesting a new low-frequency flow response comparable to panel vibrations. Another recent experiment at Mach 5.33, revealed strong flow-panel oscillation coupling and significant temperature-dependent panel stiffness effects [40]. Gaitonde and Adler [2] highlighted the amplification of frequencies below turbulent boundary layer frequencies in fluid-structure interactions, noting challenges posed by thermal wall boundary conditions and localized heating from SBLI. Despite its critical role in high-speed flow fatigue, research on thermo-elastic responses remains limited [41, 42]. Previous research efforts have largely focused on the experimental investigation of the thermo-elastic response in high-speed flows [43–46]. On the other hand, theoretical work has primarily relied on analytical methods, which offer precise but often overly simplified models, or on a combination of numerical and analytical approaches, which strive to balance computational feasibility with physical accuracy. Despite these efforts, there remains a substantial gap in comprehensive theoretical models that can accurately capture the intricate details of thermo-elastic responses in high-speed environments.

The need for advanced theoretical frameworks is underscored by the increasing complexity of modern aerospace applications, where precise control of thermal and structural interactions is crucial for performance and safety. Developing robust numerical models that can integrate thermal coupling with FSI dynamics across multiple scales will be pivotal in advancing our understanding and capability in this field. Such models would not only enhance predictive accuracy but also facilitate the design and optimization of high-speed vehicles, where thermal effects and fluid-structure interactions are critically important.

In this study, we build upon our previous work[12, 47] to explore the complex dynamics of a three-dimensional turbulent boundary layer and its interaction with a shock wave impacting a thermally active flexible surface. This research delves into the fundamental aspects of aero-thermo-elastic interactions, focusing on how an impinging shock wave penetrates the boundary layer and affects the coupled dynamics of the fluid and the flexible structure. Our primary objectives are to identify and quantify the most critical parameters influencing the dynamic behavior of a fully-coupled thermoelastic system, deepen our understanding of boundary layer dynamics under shock action over a compliant surface, and explore the turbulent interactions that occur in the presence of shock and low-frequency oscillations associated with SBLI. By investigating these aspects, we aim to uncover the mechanisms governing the aero-thermo-elastic response of the boundary layer and develop strategies for controlling and optimizing these interactions. The insights gained from this research will be crucial for improving the design and performance of high-speed vehicles, ensuring reliability and safety through precise control of thermal and structural interactions.

#### II. Formulation and computational setup

In this setup, a finite-difference flow solver and a finite-element thermal-structural solver are interconnected using the partitioned coupling approach [48]. This method involves treating each solver independently but iteratively exchanging information at defined interfaces to achieve a coupled solution.

#### A. Flow solver

A sharp-interface immersed boundary formulation is combined with a sixth-order compact central finite difference scheme for spatial discretization. A third-order total variation diminishing Runge-Kutta (RK3-TVD) method is used for spatial and temporal discretization of the flow equations, respectively [49–52]. The flow equations are nondimensionalized using the characteristic length scale of boundary layer thickness at the inflow location ( $\delta$ ), the characteristic velocity ( $U_{\infty}$ ) chosen to be the free-stream velocity, characteristic temperature ( $T_{\infty}$ ), pressure ( $P_{\infty}$ ) and density ( $P_{\infty}$ ) (based on the free stream condition and related by  $P_{\infty} = P_{\infty}RT_{\infty}$ ), and free-stream viscosity ( $P_{\infty}$ ) and conductivity ( $P_{\infty}$ ).

$$\tilde{x} = \frac{x}{\delta}, \qquad \tilde{t} = \frac{t}{\delta/U_{\infty}}, \qquad \tilde{\rho} = \frac{\rho}{\rho_{\infty}}, \qquad \tilde{u} = \frac{u}{U_{\infty}}, \qquad \tilde{p} = \frac{p}{\rho_{\infty}U_{\infty}^2}$$
 (1)

$$\tilde{T} = \frac{T}{T_{\infty}}, \qquad \tilde{E} = \frac{E}{U_{\infty}^2}, \qquad \tilde{\mu} = \frac{\mu}{\mu_{\infty}}, \qquad \tilde{\kappa} = \frac{\kappa}{\kappa_{\infty}}$$
 (2)

where,  $\rho$ , u, p, T, E,  $\mu$ , and  $\kappa$  are the density, velocity vector, pressure, temperature, total energy, viscosity, and thermal conductivity respectively. The non-dimensional symbol ( $\sim$ ) is removed hereafter for simplicity. The non-dimensional equations describing the conservation of mass, momentum, and total energy for the compressible calorically perfect gas flow are as follows,

$$\frac{\partial \rho}{\partial t} + \nabla \cdot (\rho \mathbf{u}) = 0, \tag{3}$$

$$\frac{\partial(\rho \boldsymbol{u})}{\partial t} + \boldsymbol{\nabla} \cdot \left[ \rho \boldsymbol{u} \otimes \boldsymbol{u} + p \mathbf{I} - \frac{1}{\text{Re}} \boldsymbol{\sigma}_f \right] = 0, \tag{4}$$

$$\frac{\partial (\rho E)}{\partial t} + \nabla \cdot \left[ (\rho E + p) \mathbf{u} - \frac{1}{\text{Re}} (\mathbf{\sigma}_f \odot \mathbf{u}) - \frac{1}{\text{Re Pr} (\gamma - 1) \text{Ma}} \mathbf{q} \right] = 0, \tag{5}$$

where  $\gamma = c_{P,\infty}/c_{\nu,\infty}$  is the specific heat ratio. In the equations above, the nondimensional parameters include the Mach number (Ma), Reynolds number (Re), and Prandtl number (Pr), defined as:

$$Ma = \frac{U_{\infty}}{c_{\infty}}, \qquad Re = \frac{\rho_{\infty}U_{\infty}\delta}{\mu_{\infty}}, \qquad Pr = \frac{\mu_{\infty}c_{p,\infty}}{\kappa_{\infty}}$$
 (6)

The dimensionless total energy (E) per unit mass and the nondimensional equation of state can be defined as,

$$E = \frac{p}{\rho(\gamma - 1)} + \frac{1}{2}\boldsymbol{u} \cdot \boldsymbol{u}, \qquad p = \frac{1}{\gamma M a_{\text{co}}^2} \rho T$$
 (7)

The viscous stress tensor  $\sigma$  and the heat flux q are defined as,

$$\mathbf{\sigma} = 2\left(\mu + \mu^*\right) \mathbf{S} + \left(\beta^* - \frac{2}{3}\right) (\nabla \cdot \boldsymbol{u}) \mathbf{I},$$

$$\boldsymbol{q} = -\left(\kappa + \kappa^*\right) \nabla T$$
(8)

where the strain rate tensor is,

$$\mathbf{S} = \frac{1}{2} \left[ \nabla \otimes \mathbf{u} + (\nabla \otimes \mathbf{u})^T \right] \tag{9}$$

and  $\mu$  and  $\kappa$  are the scaled dynamic viscosity and thermal conductivity, defined based on Sutherland's formula. In addition,  $\mu^*$ ,  $\beta^*$  and  $\kappa^*$  are the artificial shear viscosity, artificial bulk viscosity, and artificial thermal diffusivity defined on a non-uniform Cartesian grid as [53–56],

$$\mu^* = C_{\mu} \, \rho \, |\overline{\nabla^4 \mathbf{S}}| \Delta^6, \qquad \beta^* = C_{\beta} \, \rho \, |\overline{\nabla^4 \mathbf{S}}| \Delta^6, \qquad \kappa^* = C_{\kappa} \, \frac{\rho \, c}{T} \, |\overline{\nabla^4 \left(\frac{RT}{\gamma - 2}\right)}| \, \Delta^5$$
 (10)

where  $\Delta$  is the grid spacing. The over-bar denotes an approximate truncated-Gaussian filter. Here,  $C_{\mu} = 0.002$ ,  $C_{\beta} = 1.0$ , and  $C_{\kappa} = 0.01$  is used, as suggested by [56], and the fourth derivatives are computed by the central compact scheme [49].

#### **B. Solid Solver**

In the present study, to account for the geometric non-linearity, temperature dependency, and large deformation, the Green-Lagrangian strain tensor (**E**) and second Piola-Kirchhoff stress tensor (**S**) are defined as follows to express the stress-strain relation.

$$\mathbf{S} = \mathbf{C} : \mathbf{E}_e, \quad \mathbf{E}_e = \mathbf{E} - \mathbf{E}_T, \quad \mathbf{E} = \frac{1}{2} (\mathbf{F}^T \mathbf{F} - \mathbf{I})$$
 (11)

where, ':' represents the double dot tensor product,  $\mathbf{F}$  is the deformation gradient between the initial position and the current position, and  $\mathbf{C}$  is the elasticity/stiffness tensor which is a function of Young's modulus and Poisson ratio. To account for the temperature dependency of the shear and strain, the thermal elasticity ( $\mathbf{E}_T$ ) is considered which can be described by the following equation under the assumption that thermal strain is very small compared to the strain due to the external loading, as

$$\mathbf{E}_T = \alpha (T - T_{\text{ref}}) \tag{12}$$

where  $\alpha$  is the coefficient of thermal isotropic expansion.

In the solid region, the nondimensional equation of motion can be written based on the Cauchy number  $C_a$  and the mass number  $M^*$  as,

$$\frac{d^2 \mathbf{d}}{dt^2} = \frac{M^*}{C_a} \nabla \cdot \mathbf{\sigma}_s + \mathbf{f}_s, \quad C_a = \frac{\rho_\infty U^2}{E}, \quad M^* = \frac{\rho_\infty}{\rho_s}$$
 (13)

where,  $\sigma_s$  is the nondimentional Cauchy stress tensor, E is the Young's modulus of the solid material and  $f_s$  is the nondimentional body forces per unit mass.

In the structural model, the panel is considered as a conductive material with a small thermal expansion coefficient. Then transient heat conduction problem in the compliant surface can be represented by the local heat balance equation as follows,

$$c_V \frac{\partial T_s}{\partial t} + \nabla \cdot \boldsymbol{q}_s - Q = 0 \tag{14}$$

where  $c_V$  is a characteristic property of a solid material and Q is the heat generation rate per unit volume of the solid by various deformation and chemical processes (for example as work of viscous stresses). The heat generation due to deformation, compression, or expansion is insignificant for the range of stress changes anticipated in this study and hence is not considered in this model. The heat flux  $(q_s)$  is governed by Fourier law,  $q_s = -\kappa(\nabla T_s)$ , where  $\kappa$  is  $3 \times 3$  generalized thermal conductivity matrix. The unsteady heat conduction equation shown above is discretized and solved by a linear finite element and a trapezoidal time integration scheme.

The governing equations are solved by the Galerkin finite-element (FE) method, implemented in Tahoe, an open-source, Lagrangian, three-dimensional, finite-element solver [57]. Finite element discretization yields the following system of ordinary differential equations for the nodal displacement X, at the time step n,

$$\mathbf{M}\ddot{\mathbf{X}} + \mathbf{C}\dot{\mathbf{X}} + \mathbf{R}(\mathbf{X}) = \mathbf{F}_{s} \tag{15}$$

where, M & C are coefficient matrices and R(X) is the geometrically nonlinear stiffness term. The Hilber-Hughes-Taylor (HHT) time integration scheme [58] is used for temporal discretization. If  $A_n, V_n$ , and  $D_n$  are given approximation for  $\ddot{X}(t_n), \dot{X}(t_n)$  and  $X(t_n)$ , it can be written that

$$D_{n+1} = D_n + \Delta t V_n + \Delta t^2 \left[ \left( \frac{1}{2} - \beta \right) A_n + \beta A_{n+1} \right]$$

$$V_{n+1} = V_n + \Delta t \left[ (1 - \gamma) A_n + \gamma A_{n+1} \right]$$
(16)

and a one-step approximation to Eq. 15 can be formed as

$$\mathbf{M}A_{n+1} + \mathbf{C}V_{n+1-\alpha_f} + \mathbf{R}(\mathbf{D})_{n+1-\alpha_f} = \mathbf{F}(t_{n+1-\alpha_f})$$
 (17)

where,

$$t_{n+1-\alpha_f} = (1 - \alpha_f)t_n + \alpha_f t_{n+1}$$

$$\mathbf{R}_{n+1-\alpha_f} = (1 - \alpha_f)\mathbf{R}_n + \alpha_f \mathbf{R}_{n+1}$$

$$V_{n+1-\alpha_f} = (1 - \alpha_f)V_n + \alpha_f V_{n+1}$$
(18)

The coefficients are selected to reach an unconditionally stable and second-order accurate prediction while allowing the energy dissipation of high wave-number modes. In particular,  $\alpha$ ,  $\beta$  and  $\gamma$  are selected as  $\alpha \in [-1/3, 0]$ ,  $\gamma \in (1 - 2\alpha)/2$  and  $\beta \in (1 - \alpha)^2/4$ .

# C. Boundary and Interface Conditions

The sharp interface immersed boundary method (IBM) is used for the fluid-thermal-structure coupling. The thermal and dynamic load acting on the interface are computed by adopting the high-order immersed boundary method (IBM) formulation. For further details please refer to our previous publication [47].

## 1. Turbulent inflow generation

The inflow turbulence generation method has been a key issue in spatially evolving turbulent flow simulation. Velocity fluctuations at the inlet can be generated using the sampling approach from the precalculated turbulent spectra and with the help of the synthetic digital filtering (DF) approach [59]. The filtering operation is separated into a sequence of fast one-dimensional convolutions. The implementation requires the specification of the Reynolds stress tensor at the inflow plane, which is interpolated by a dataset of the previous DNS of the supersonic boundary layer. Initially, a mean fully developed turbulent compressible boundary layer was obtained by applying the van Driest transformation to an incompressible profile of the Musker family. This approach is employed for current 3D flow simulations.

#### 2. Shock and Outflow sponge layer

The Rankine–Hugoniot conditions, also referred to as Rankine–Hugoniot jump conditions, are used for generating shock at the top surface of the domain such that the oblique shock hits the flexible panel in the middle. A sponge region is added to reduce reflections from the outflow boundaries [60]. The damping parameters of the sponge region are adjusted through trial and error such that the reflectivity of sponge zones is minimized [61].

## 3. Kinematics conditions at the wall and the interface

At the interface, to impose no-slip boundary conditions and ensure dynamic equilibrium, the traction force between the structure and flow balanced as follows,

$$\mathbf{\sigma}_{\mathbf{s}} \cdot \mathbf{n} = \mathbf{\sigma}_{f} \cdot \mathbf{n} \tag{19}$$

where  $\sigma_f = -pI + \tau$  and for higher Reynolds numbers, the second term  $(\tau)$  can be ignored. The kinematic boundary condition at the interface, to ensure no-slip condition, is expressed as  $u_f = \partial d/\partial t$ , where u and d are the velocity of the fluid and displacement of the solid at the interface, respectively.

# 4. Thermoelastic coupling

For two-way thermally coupled simulations, the rigid wall is assumed to be isothermal at the recovery temperature. For the flexible part, the thermal condition has been satisfied at the interface of the panel and fluid by assuming zero net heat flux at the interface, which leads to  $(\mathbf{q}_s + \mathbf{q}_f) \cdot \mathbf{n} = 0$ . Because of the no-slip condition, the wall temperature is the same for both the solid and fluid  $(T_f = T_s)$  at the interface.

#### D. Solver coupling algorithm

In the current solution algorithm, the process begins by solving the flow field based on the existing thermal and kinematic conditions at the fluid-solid interface. This involves calculating the thermal and dynamic loads acting on the interface using a high-order immersed boundary method (IBM) formulation [62]. These loads are then used to determine the flow quantities at the interface.

With the interface conditions established, the algorithm proceeds to iteratively compute the dynamic deformation and thermal response of the solid. This is treated as a strongly coupled nonlinear system of equations, which is solved repeatedly until a specified convergence criterion is met. During this iterative process, the thermal and dynamic boundary conditions are continually updated to reflect the interactions between the fluid and the solid.

Once the algorithm converges and the thermal and dynamic states of the solid are accurately determined, the updated kinematic and thermal conditions are transferred back to the flow solver. This updated information is used to initiate the new time step, ensuring that the solution accurately reflects the evolving interactions between the fluid and the solid.

Table 1 Validation cases

Case number	Panel type	Inflow type	Flow type	$Re_{\tau}$	Grid
TBL-Rf	Rigid	Turbulent	ZPG BL	300	$2041 \times 256 \times 225$
STBLI-Rf	Rigid	Turbulent	SBLI	300	$2041 \times 256 \times 225$

The entire solution procedure is a dynamic, iterative process that integrates the thermal and mechanical responses of the solid with the fluid flow characteristics, ensuring a comprehensive and accurate simulation of the fluid-structure interaction. This process is depicted in a simplified manner in Fig. 1, illustrating the sequential steps and the iterative process of the solution algorithm.

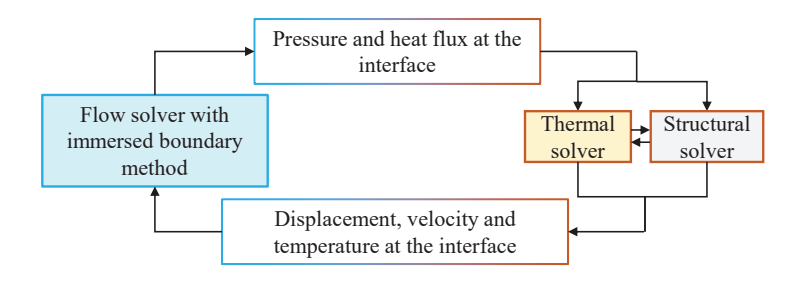


Fig. 1 Fluid-thermal-structure interaction (FTSI) algorithm.

The coupling strategy implemented in the structural solver considers two material models: (1) a heat transfer model and (2) a structural mechanics model. The iterative algorithm operates by first solving the temperature field of the solid using the heat transfer model, followed by predicting the material temperature to solve for deformation using the structural mechanics model until the residuals meet the convergence criterion. Throughout this process, the physical system assumes that thermal-induced stresses may affect the structure, but the temperature field remains unaffected by deformation, implying negligible heat generation from continuous rapid deformations.

## III. Results

3D simulations have been conducted for Mach 2 flow with an incoming laminar and turbulent boundary layer with and without impinging shock. For SBLI cases, a shock generated from the top boundary at a specified angle hits the boundary at  $x - x_0/\delta = 0.0$  (midpoint of the panel for flexible cases), where  $x_0$  is the shock impingement location and  $\delta$  is incoming boundary layer thickness. The domain is extended from  $-34\delta$  to  $32\delta$  in the streamwise direction (x-axis) and the shock hits at the center  $x/\delta = 0.0$ . The domain is spanned from  $-3.5\delta$  to  $3.5\delta$  (z-axis) and extends between 0.0 to  $12\delta$  in the wall-normal direction (y-axis).

For the validation cases, the friction Reynolds number  $(Re_{\tau})$  is 300. The shock angle is 39° corresponds to a pressure jump of 1.68 across the shock.

For flexible cases, the friction Reynolds number  $(Re_{\tau})$  is 150 and the Reynolds number  $(Re_{\delta})$  is 7190 based on the incoming boundary layer thickness  $(\delta_{99})$ . The 35° shock angle corresponds to a pressure jump of 1.4 across the shock. The flexible panel extends from  $x/\delta = -7.5$  to  $x/\delta = 7.5$  and  $z/\delta = -2.5$  to  $x/\delta = 2.5$  with a thickness of  $0.5\delta$ . The Young modulus  $(E/\rho_{\infty}U_{\infty}^2)$ , density  $(\rho_s/\rho_f)$ , and Poisson ratio  $(\nu)$  of the flexible panel are 1000, 500, and 0.45, respectively. For flexible panel cases, the cavity pressure beneath the panel (bottom wall pressure,  $P_{bw}$ ) is the average pressure across the shock.

## A. Validation study

# 1. Turbulent boundary layer over rigid wall

For verification purposes, turbulent boundary layer flow has been simulated over a rigid adiabatic surface. The simulation parameters used for validation are listed in Table 1. Simulations were conducted with a finer mesh resolution

Cavity Case Panel Inflow Reynolds Cavity Grid temperature number number pressure type type  $(T_{bw}/T_{\infty})$ STBLI-Rc Rigid Turbulent  $Re_{\tau} = 150$  $511 \times 226 \times 53$  $p_{\infty}$ Flexible  $Re_{\delta} = 7000$  $511 \times 226 \times 53$ SLBLI-Fc Laminar  $p_{\infty}$ Flexible- $Re_{\tau} = 150$ STBLI-Fc  $511 \times 226 \times 53$ Turbulent  $P_{bw}$ Adiabatic Flexible-STBLI-FCc Turbulent  $Re_{\tau} = 150$  $511 \times 226 \times 53$  $P_{bw}$ 1.0 Cooling Flexible-

 $Re_{\tau} = 150$ 

Turbulent

Heating

 $511 \times 226 \times 53$ 

 $P_{bw}$ 

2.0

Table 2 Parameters of FTSI of STBLI cases

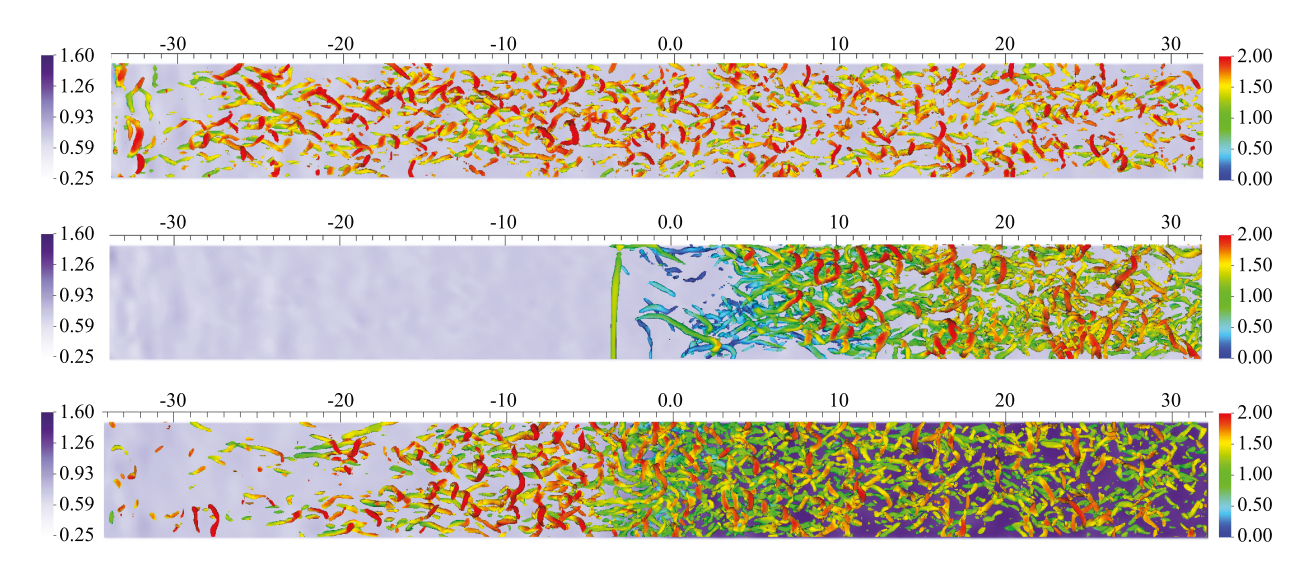


Fig. 2 Near boundary flow structures for (a) turbulent boundary layer, (b) transitional SBLI, and (c) turbulent SBLI. The background contour plot is pressure and iso-surface is the Q-criterion colored with velocity magnitude

where y+ is 0.6. The Q-criterion of the instantaneous flow field is depicted in Fig. 2 (a). The van Driest average velocity profile is compared against the Ref. [59] in Fig. 3. The results (both the velocity profile and Reynolds stresses) show reasonable agreement with the literature in Fig. 3. Please note that the Favre average is denoted by  $\widetilde{(\cdot)}$  and the Reynolds average is denoted by  $\overline{(\cdot)}$ .

# 2. STBLI over rigid wall

STBLI-FHc

Another test was conducted for the same grid resolution and flow conditions with an impinging oblique shock interacting with the incoming turbulent boundary layer. The instantaneous and average density gradient has been shown in Fig. 4. The flow field shows a slight increase in the incoming boundary layer as it crosses the interaction zone. In the average flow field, the reflected and reattachment shock is clearly identifiable.

In addition to evaluating the solver's accuracy, the FSI and FTSI coupling algorithm between the flow and solid solvers has also been extensively validated in our previous study [47].

# B. Laminar/transitional SBLI over adiabatic rigid/flexible wall

For a systematic investigation, at first, we reiterate the behavior of SBLI over a rigid surface with the turbulent boundary layer (Case STBLI-Rc in Table 2). Later, we briefly explored the impact of the shock on the laminar boundary layer (Case STBLI-Fc in Table 2). As soon as the shock hits the incoming laminar boundary layer, it initiates the

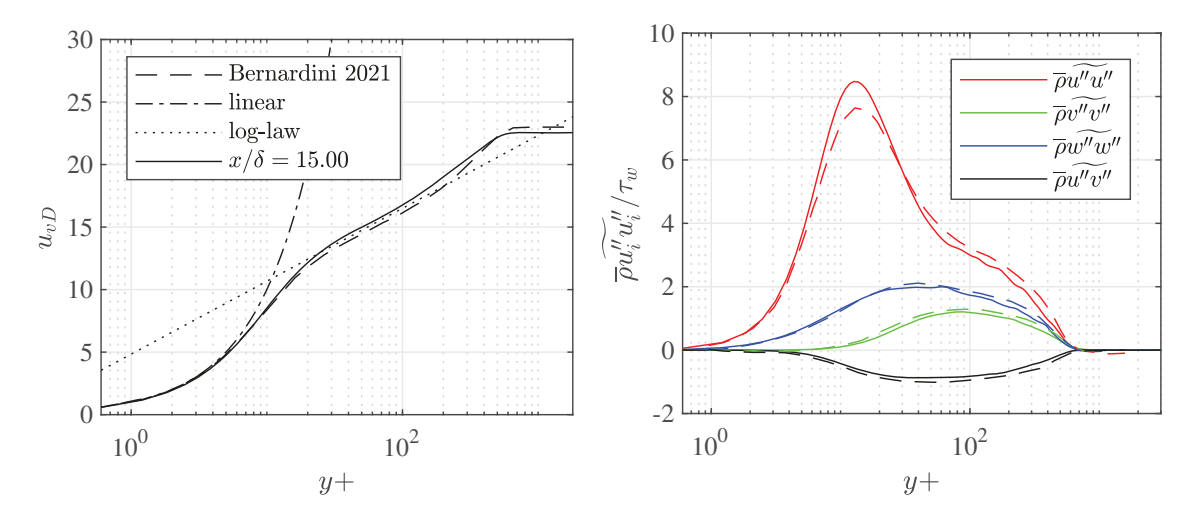


Fig. 3 Time-averaged (a) van Driest velocity profile and (b) Reynolds stresses (solid lines: present study at station  $x/\delta = +25.00$ , dashed lines: Ref. [59])

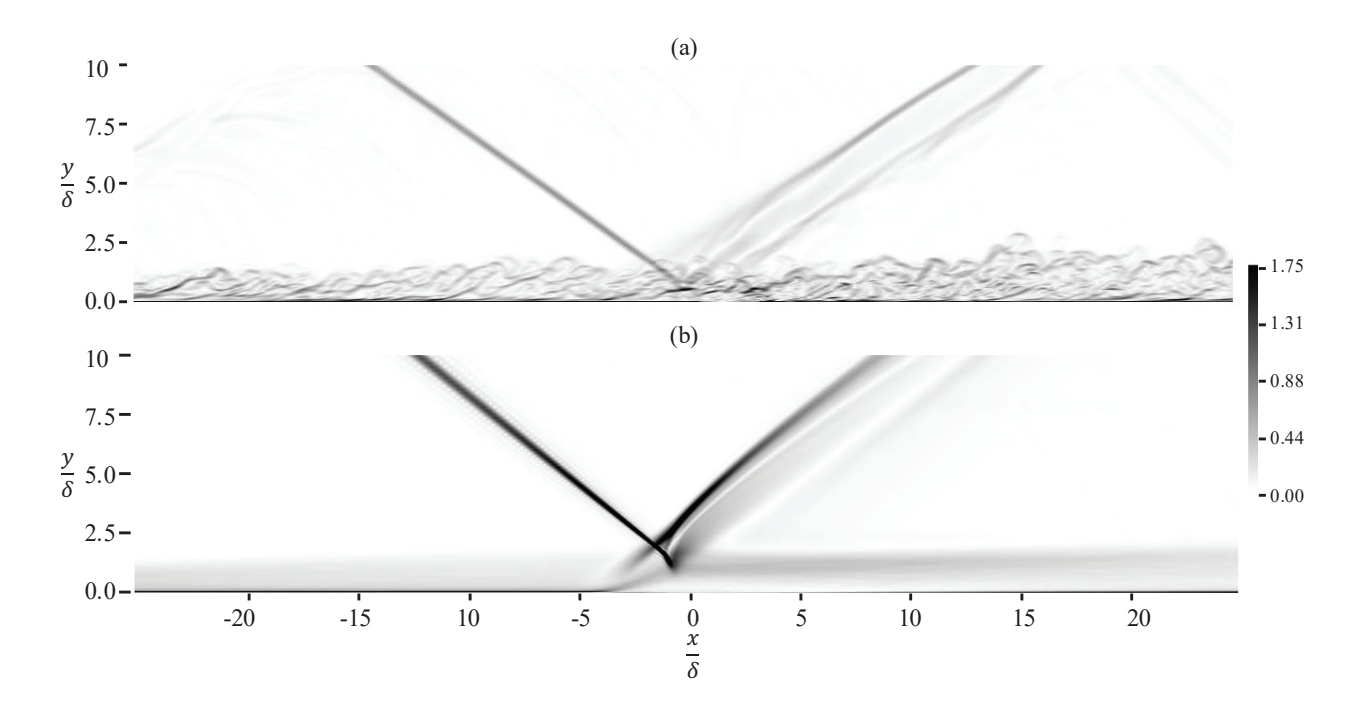


Fig. 4 (a) Instantaneous and (b) time-averaged density gradient for STBLI over the rigid surface

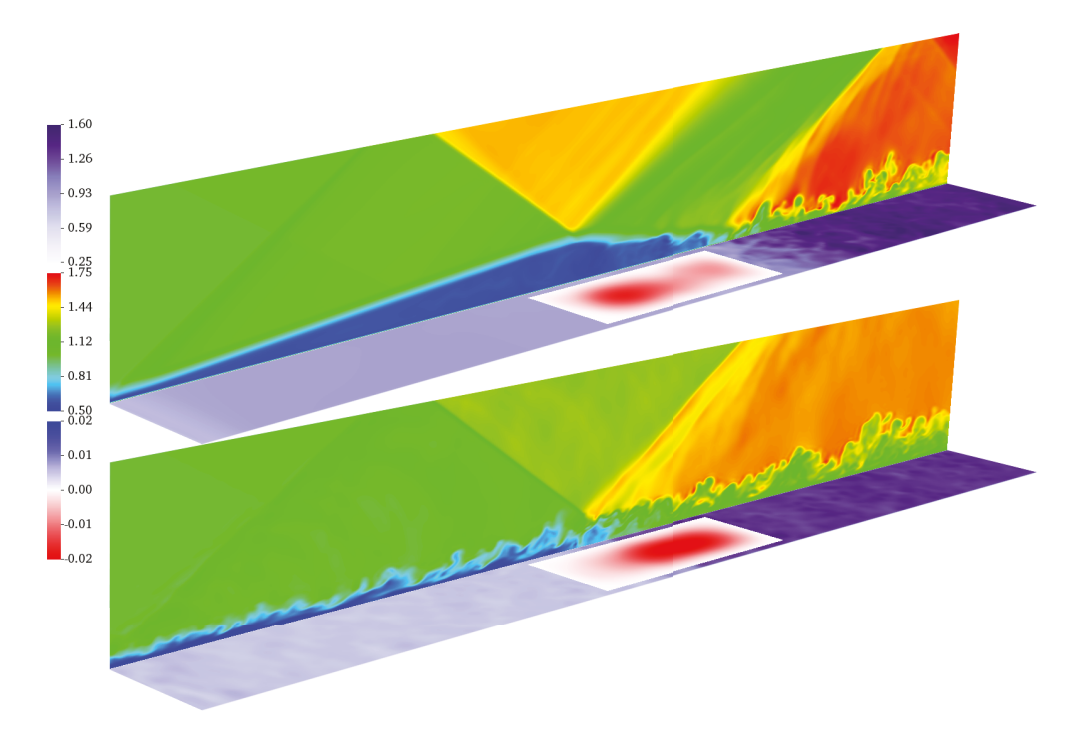


Fig. 5 Instantaneous results of shock wave boundary layer interaction over the flexible panel with (a) laminar and (b) turbulent inflow. [Blue-Green-Red] Instantaneous density contour slice at  $z/\delta = -3.1$ ; [Purple-White] surface pressure; [Blue-White-Red] panel deflection normalized by boundary layer thickness.

transition to turbulence. Figure 2(b) shows the formation of the turbulent coherent structures e.g. hairpin vortices downstream of the shock impingement location ( $x/\delta = 0.0$ ). The density contour of the flow field has been shown in Fig. 5(a). For turbulent cases in Fig. 5(b), the separation bubble and the interaction region are considerably smaller than in the laminar case. The laminar SBLI has a larger separation bubble than the turbulent case. The reattachment point has been shifted downstream and a wider expansion fan region can be seen. However, the contribution of the flexible panel to the transition is yet to be evaluated and is not in the scope of our current investigation.

## C. Turbulent SBLI over adiabatic flexible wall

First, we also briefly studied the shockwave turbulent boundary layer interaction over the rigid wall (Case STBLI-Fc in Table 2), and the density gradient of the flow field is shown in Fig 4. The shock causes a thicker boundary layer downstream of the shock impingement location along with the formation of the separation bubble as seen in Fig. 4.

To investigate the impact of panel flexibility on the boundary layer statistics, the Reynolds stress for both rigid and flexible panels is compared in Fig. 6 at upstream  $(x/\delta=-10)$ , mid-panel  $(x/\delta=0)$ , and downstream  $(x/\delta=10)$  location. The interplay of aerodynamic forces, the kinetic energy of the panel, and the restoring potential elastic energy is mainly responsible for the panel oscillation. The impact of the oscillation is mainly reflected in the streamwise fluctuating component of the velocity. However, in this case, the upstream and downstream impact of the panel oscillation is very negligible. The Reynolds stress profiles downstream of the shock impingement location have deviated from the regular boundary layer profile.

The flow field in Fig. 5(b), depicting instantaneous density, is characterized by an impinging shock, reflected and separation shock, an expansion fan, a separation bubble, and turbulent structures on the boundary layer. Comparing the turbulent intensities in Fig. 6, the flexible panel mostly changes the profile in the buffer region of the boundary layer. The streamwise and spanwise turbulent intensity profiles have deviated most from the rigid SBLI case. From Fig. 6(a) and (c), it can be asserted that the profile before and after the interaction zone matches closely with the rigid case, while only the zone directly above the flexible part of the panel is impacted. The impacts of the panel motion quickly dissipate downstream.

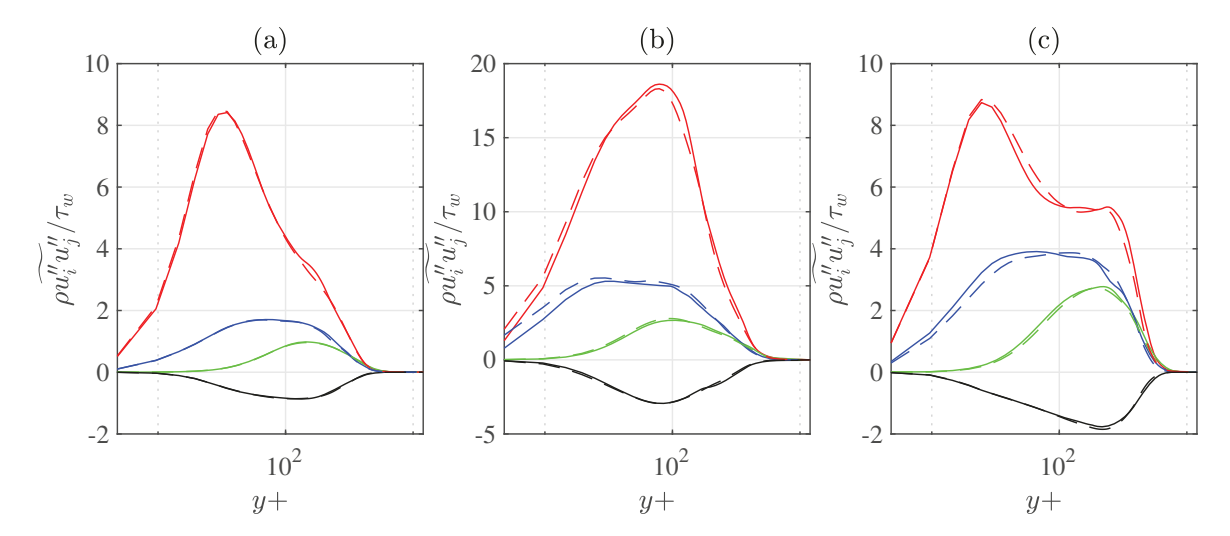


Fig. 6 Time-averaged Reynolds stresses (solid lines: rigid, dashed lines: flexible-adiabatic) at (a) upstream  $x/\delta = -10.0$ , (b) mid-panel  $x/\delta = 0.0$  and (c) downstream  $x/\delta = +10.0$ . For legend, please refer to Fig. 3(b).

## D. Turbulent SBLI of fully-coupled non-adiabatic thermoelastic wall

Later, we evaluated the behavior of the flexible panel coupled with the temperature. In this setup, the bottom wall of the panel is kept at a constant temperature while only the top surface interacts with the flow. The temperature of the side walls is kept constant at the recovery temperature. The non-dimensional thermal properties of the solid panel are selected from our previous study [47]. The non-dimensional specific heat  $(C_{p_s}T_{\infty}/U^2)$  of the panel is  $2.1 \times 10^{-3}$  and thermal expansion coefficient  $(\alpha_{\Delta}T_{\infty})$  is  $3.7 \times 10^{-3}$ . The other parameters are listed in Table 2 (Case STBLI-FCc and STBLI-FHc).

#### 1. Interaction over cold wall

To evaluate the impact of the panel temperature along with flexibility, another simulation was conducted where the bottom temperature of the panel is kept constant at  $T_{bw}/T_{\infty} = 1.0$ . Since  $T_{bw}/T_{\infty}$  is smaller than the recovery temperature which is  $T_r/T_{\infty} = 1.68$ , it will induce a cooling effect. Unlike the flexible case, the cooling significantly affects both the viscous sublayer and buffer region above the panel in Fig. 7(b). A colder wall increases the density of the adjacent fluid, thereby enhancing the average momentum flux into the boundary layer [63].

The wall-normal deflection of the panel at  $z/\delta = 0.0$  (a line drawn on the top surface of the panel along the streamwise direction) has been shown in Fig. 8 for adiabatic, cooling, and heating cases. As time progresses, the panel reaches a mean deflection and oscillates around the mean position. Comparing the adiabatic and cooling cases, the timescale of the panel oscillation is significantly higher in the cooling case. The amplitude of the panel oscillation is larger in the cooling case.

The panel's oscillation shows different modes of deflection as shown in Fig. 9. The first mode shows the most dominant form of the deformation, which is weighted more downstream since the shock has higher pressure on the downstream side. The fifth mode shows low-frequency oscillation. Higher mode shapes are responsible for transverse deformation. Though initially higher modes (third and more) are submissive, they become important as the simulation progresses into a pseudo-steady state.

# 2. Interaction over heated wall

Since the heated wall leads to the increase of the boundary layer thickness, we have observed a slight upstream influence of the boundary layer as seen in Fig. 10(a). Likewise the cooling case, the main impact of the panel temperature and oscillation is observed on the streamwise component of the Reynolds stresses. Comparing the cooling effect, the heating has much less impact on the streamwise Reynolds stress in the laminar sublayer region. For this case, the magnitude of the panel oscillation is also higher than the adiabatic case. The effective elasticity of the solid decreases as the temperature increases. The lower stiffness is responsible for, the higher amplitude of the panel. Similarly, Daub et al. observed that heating reduces the stiffness of a prestressed panel, resulting in larger deflections [40].

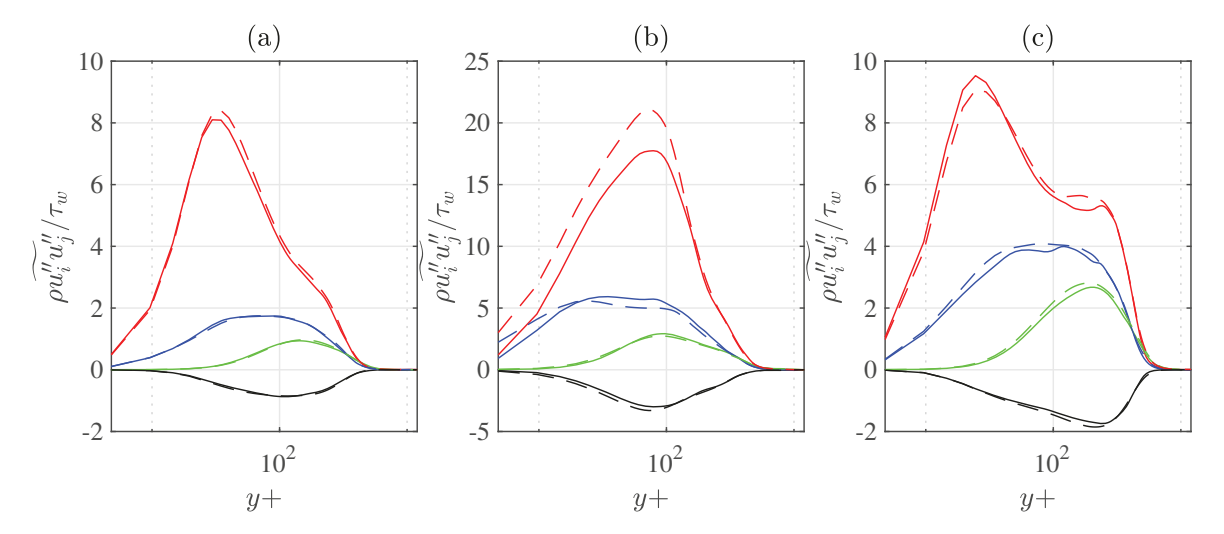


Fig. 7 Time-averaged Reynolds stresses (solid lines: rigid, dashed lines: cooling) at (a) upstream  $x/\delta = -10.0$ , (b) mid-panel  $x/\delta = 0.0$  and (c) downstream  $x/\delta = +10.0$ . For legend, please refer to Fig. 3(b).

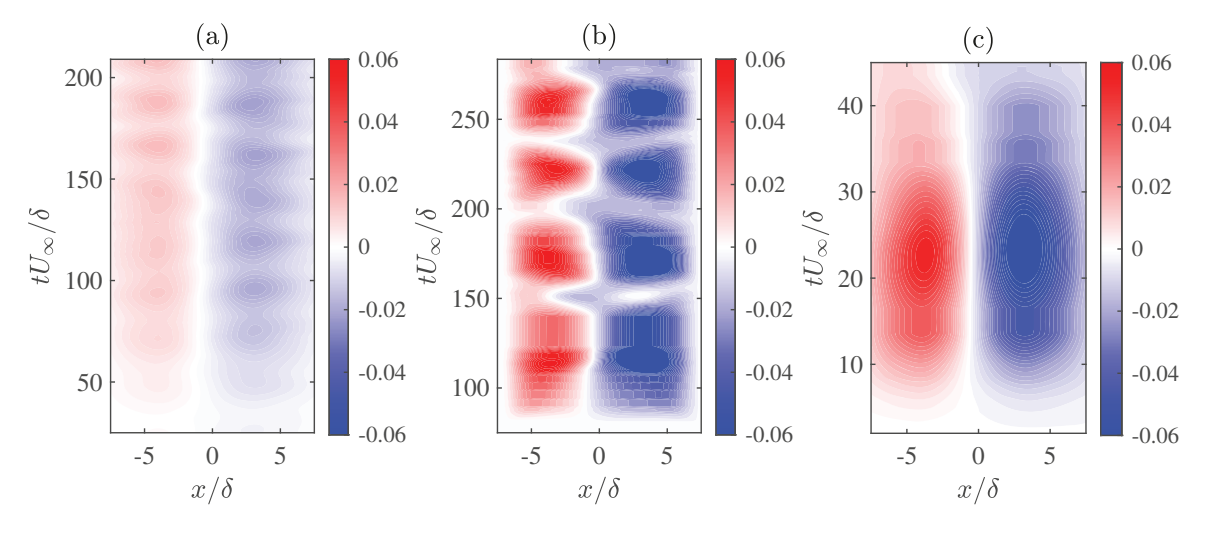


Fig. 8 Wall-normal deformation of the panel for (a) adiabatic, (b) cooling, and (c) heating at  $z/\delta = 0.0$ .

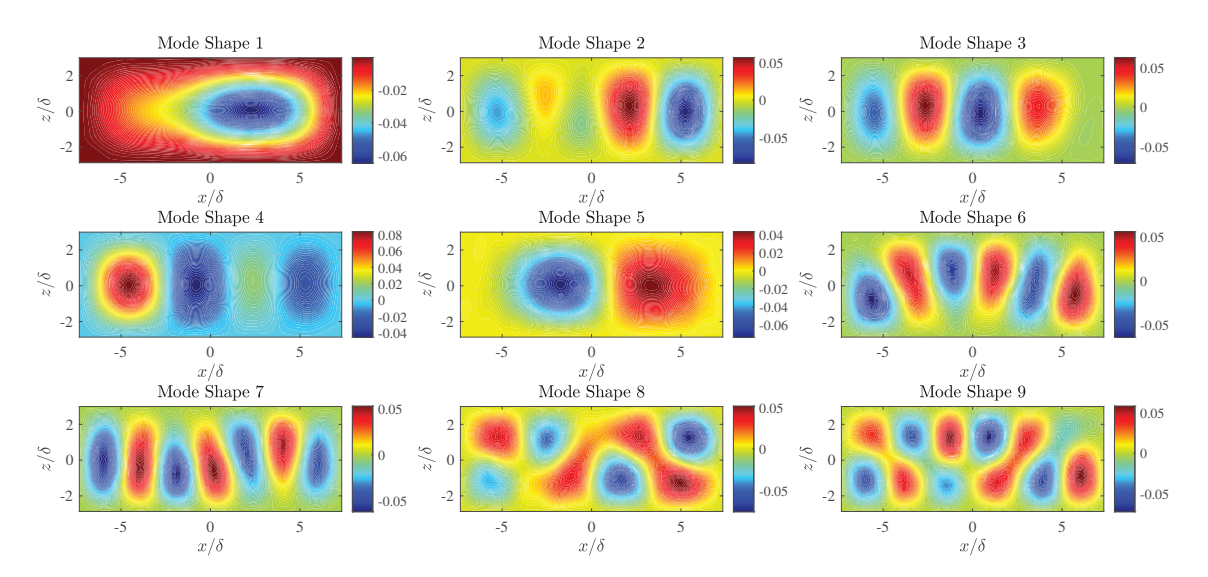


Fig. 9 Mode shape of the surface deformation for Case STBLI-Fc

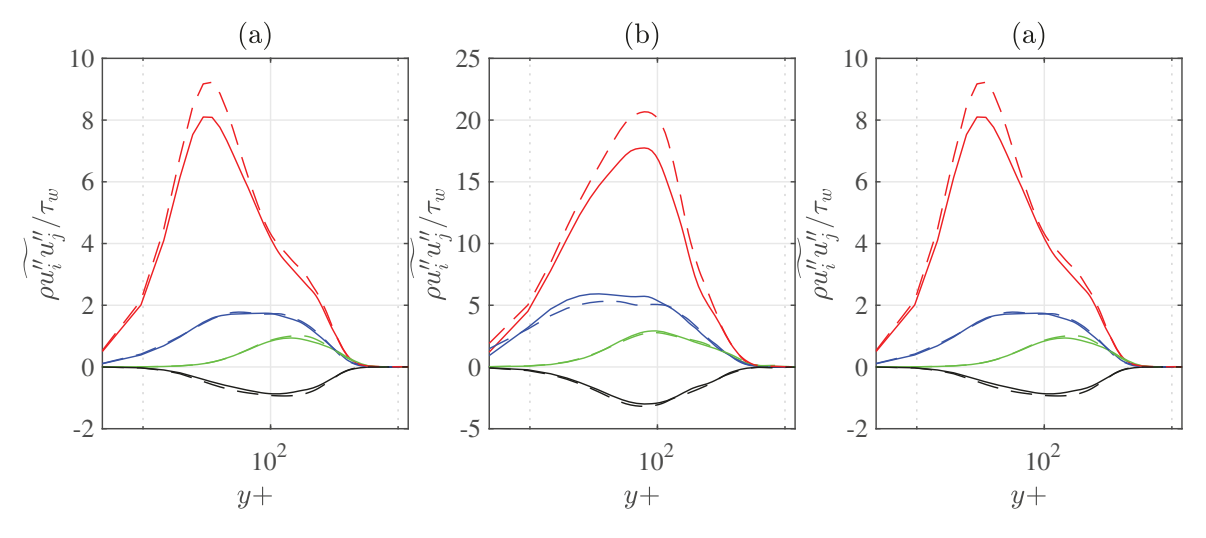


Fig. 10 Time-averaged Reynolds stresses (solid lines: rigid, dashed lines: heating) at (a) upstream  $x/\delta = -10.0$ , (b) mid-panel  $x/\delta = 0.0$  and (c) downstream  $x/\delta = +10.0$ . For legend, please refer to Fig. 3(b).

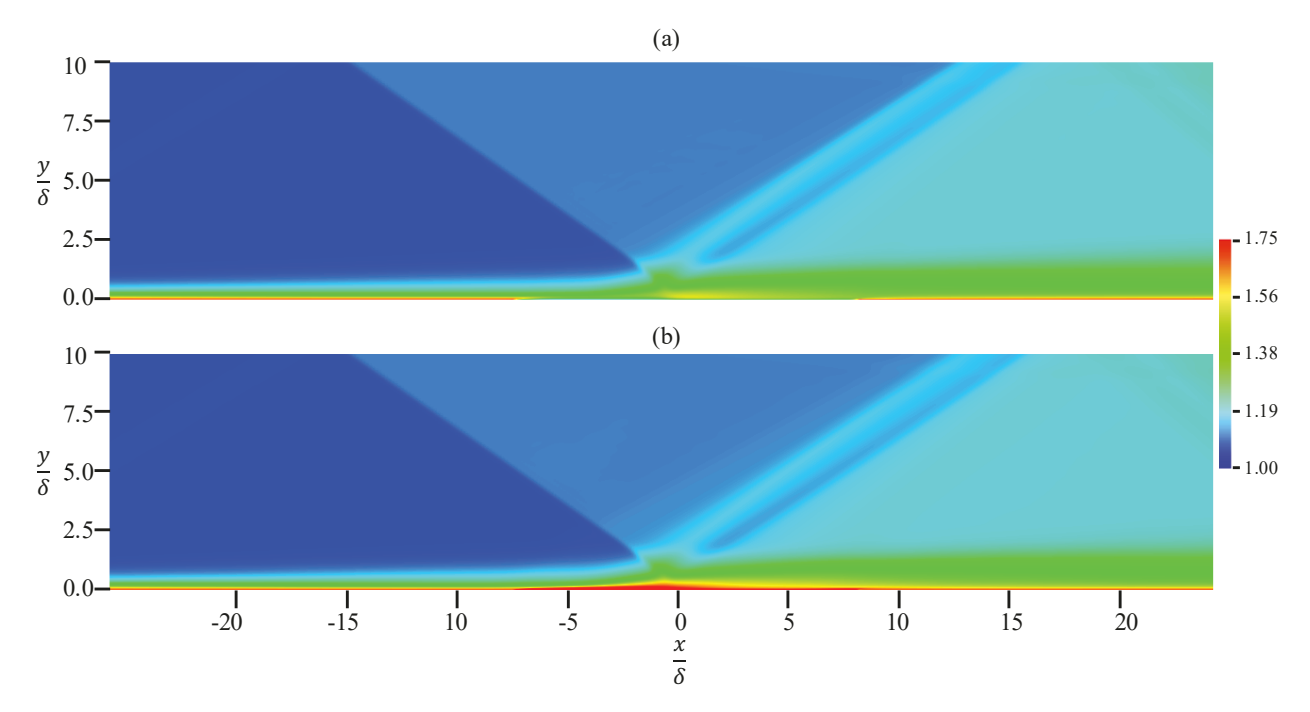


Fig. 11 Time-averaged temperature for STBLI under (a) cooling and (b) heating effect.

The time-averaged temperature field is shown in Fig. 11 for both the cooling and heating effects to assess the qualitative impact on the interaction zone. For the turbulent boundary layer, the panel temperature locally influences the interaction region. In the turbulent boundary layer, the impact of the panel motion and temperature on the surface properties downstream of the separation zone diminishes quickly.

#### IV. Conclusion

This study examines the impact of aero-thermo-elastic interactions on shock wave boundary layer interaction (SBLI) over an elastic structure under different thermal conditions. The shock induces an early transition to turbulence for the laminar flow case and the quantitative contribution of flexible panel in the transition process is yet to be measured. Results for shockwave and turbulent boundary layers over rigid and flexible panels for different cavity temperatures have been discussed. We have observed significant differences in the behavior of the flexible panel when solid properties are not independent of temperature. The Reynolds shear stress for adiabatic, cooling, and heating has been compared. The 3D coherent and turbulent structure is greatly impacted by the FTSI system. This study shows that the interaction between the compliant panel and thermal conditions can significantly alter the panel's oscillatory behavior, exceeding the impact of each factor alone. Fluid-structural-thermal interactions in high-speed flows are inherently complex and non-linear. Various influential parameters, such as cavity pressure, Young's modulus, thermal expansion coefficient, and specific heat, can significantly alter the effective excitation of shock-induced fluttering, necessitating more detailed study.

## Acknowledgments

This study is funded by the Defense Advanced Research Projects Agency (DARPA) under Grant No. D19AP00035 and the National Science Foundation (NSF) under Award No. 2341192. The authors also acknowledge the support of the Research Computing Center at Florida State University for providing the necessary resources to conduct the research reported in this paper.

## References

- [1] Gaitonde, D. V., "Progress in shock wave/boundary layer interactions," *Progress in Aerospace Sciences*, Vol. 72, 2015, pp. 80–99.
- [2] Gaitonde, D. V., and Adler, M. C., "Dynamics of Three-Dimensional Shock-Wave/Boundary-Layer Interactions," *Annual Review of Fluid Mechanics*, Vol. 55, 2022.
- [3] Niessen, S., "BiGlobal Stability Analysis: Laminar Shock-Wave/Boundary-Layer Interactions,", Aug 2017.
- [4] Délery, J., and Dussauge, J.-P., "Some physical aspects of shock wave/boundary layer interactions," Shock Waves, Vol. 19, No. 6, 2009, p. 453.
- [5] Dolling, D. S., "Fifty years of shock-wave/boundary-layer interaction research: what next?" *AIAA journal*, Vol. 39, No. 8, 2001, pp. 1517–1531.
- [6] Babinsky, H., and Harvey, J. K., Shock wave-boundary-layer interactions, Vol. 32, Cambridge University Press, 2011.
- [7] Pagella, A., Rist, U., and Wagner, S., "Numerical investigations of small-amplitude disturbances in a boundary layer with impinging shock wave at Ma= 4.8," *Physics of Fluids*, Vol. 14, No. 7, 2002, pp. 2088–2101.
- [8] Benay, R., Chanetz, B., Mangin, B., Vandomme, L., and Perraud, J., "Shock wave transitional boundary-layer interactions in hypersonic flow," *AIAA journal*, Vol. 44, No. 6, 2006, pp. 1243–1254.
- [9] Robinet, J.-C., "Bifurcations in shock-wave/laminar-boundary-layer interaction: global instability approach," *Journal of Fluid Mechanics*, Vol. 579, 2007, pp. 85–112.
- [10] Guiho, F., Alizard, F., and Robinet, J.-C., "Instabilities in oblique shock wave/laminar boundary-layer interactions," *Journal of Fluid Mechanics*, Vol. 789, 2016, pp. 1–35.
- [11] Gs, S., Dwivedi, A., Candler, G. V., and Nichols, J. W., "Global linear stability analysis of high speed flows on compression ramps," 47th AIAA Fluid Dynamics Conference, 2017, p. 3455.
- [12] Shahriar, A., Shoele, K., and Kumar, R., "Aero-thermo-elastic Simulation of Shock-Boundary Layer Interaction over a Compliant Surface," *AIAA Aviation Forum*, 2018, p. 3398.
- [13] Sansica, A., Sandham, N., and Hu, Z., "Forced response of a laminar shock-induced separation bubble," *Physics of fluids*, Vol. 26, No. 9, 2014, p. 093601.
- [14] Ganapathisubramani, B., Clemens, N., and Dolling, D., "Effects of upstream boundary layer on the unsteadiness of shock-induced separation," *Journal of Fluid Mechanics*, Vol. 585, 2007, pp. 369–394.
- [15] Wu, M., and Martin, M. P., "Direct numerical simulation of supersonic turbulent boundary layer over a compression ramp," *AIAA journal*, Vol. 45, No. 4, 2007, pp. 879–889.
- [16] Touber, E., and Sandham, N. D., "Large-eddy simulation of low-frequency unsteadiness in a turbulent shock-induced separation bubble," *Theoretical and Computational Fluid Dynamics*, Vol. 23, No. 2, 2009, pp. 79–107.
- [17] Nichols, J. W., Larsson, J., Bernardini, M., and Pirozzoli, S., "Stability and modal analysis of shock/boundary layer interactions," *Theoretical and Computational Fluid Dynamics*, Vol. 31, No. 1, 2017, pp. 33–50.
- [18] Priebe, S., and Martín, M. P., "Low-frequency unsteadiness in shock wave–turbulent boundary layer interaction," *Journal of Fluid Mechanics*, Vol. 699, 2012, pp. 1–49.
- [19] Piponniau, S., Dussauge, J.-P., Debieve, J.-F., and Dupont, P., "A simple model for low-frequency unsteadiness in shock-induced separation," *Journal of Fluid Mechanics*, Vol. 629, 2009, pp. 87–108.
- [20] Pirozzoli, S., and Grasso, F., "Direct numerical simulation of impinging shock wave/turbulent boundary layer interaction at M= 2.25," *Physics of Fluids*, Vol. 18, No. 6, 2006, p. 065113.
- [21] Sandham, N., Schülein, E., Wagner, A., Willems, S., and Steelant, J., "Transitional shock-wave/boundary-layer interactions in hypersonic flow," *Journal of Fluid Mechanics*, Vol. 752, 2014, pp. 349–382.
- [22] Shinde, V., McNamara, J. J., Gaitonde, D. V., Barnes, C. J., and Visbal, M. R., "Panel Flutter Induced by Transitional Shock Wave Boundary Layer Interaction," 2018 Fluid Dynamics Conference, 2018, p. 3548.

- [23] Agostini, L., Larchevêque, L., Dupont, P., Debiève, J.-F., and Dussauge, J.-P., "Zones of influence and shock motion in a shock/boundary-layer interaction," AIAA journal, Vol. 50, No. 6, 2012, pp. 1377–1387.
- [24] Aubard, G., Gloerfelt, X., and Robinet, J.-C., "Large-eddy simulation of broadband unsteadiness in a shock/boundary-layer interaction," *AIAA journal*, Vol. 51, No. 10, 2013, pp. 2395–2409.
- [25] Grilli, M., Schmid, P. J., Hickel, S., and Adams, N. A., "Analysis of unsteady behaviour in shockwave turbulent boundary layer interaction," *Journal of Fluid Mechanics*, Vol. 700, 2012, pp. 16–28.
- [26] Garnier, E., "Stimulated detached eddy simulation of three-dimensional shock/boundary layer interaction," Shock waves, Vol. 19, No. 6, 2009, p. 479.
- [27] Fang, J., Yao, Y., Li, Z., and Lu, L., "Investigation of low-dissipation monotonicity-preserving scheme for direct numerical simulation of compressible turbulent flows," *Computers & Fluids*, Vol. 104, 2014, pp. 55–72.
- [28] Wu, M., and Martin, M. P., "Analysis of shock motion in shockwave and turbulent boundary layer interaction using direct numerical simulation data," *Journal of Fluid Mechanics*, Vol. 594, 2008, pp. 71–83.
- [29] Ostoich, C. M., Bodony, D. J., and Geubelle, P. H., "Interaction of a Mach 2.25 turbulent boundary layer with a fluttering panel using direct numerical simulation," *Physics of Fluids*, Vol. 25, No. 11, 2013, p. 110806.
- [30] Vedeneev, V. V., "Panel flutter at low supersonic speeds," Journal of fluids and structures, Vol. 29, 2012, pp. 79–96.
- [31] Sander, G., Bon, C., and Geradin, M., "Finite element analysis of supersonic panel flutter," *International Journal for Numerical Methods in Engineering*, Vol. 7, No. 3, 1973, pp. 379–394.
- [32] Visbal, M., "On the interaction of an oblique shock with a flexible panel," *Journal of Fluids and structures*, Vol. 30, 2012, pp. 219–225.
- [33] Visbal, M., "Viscous and inviscid interactions of an oblique shock with a flexible panel," *Journal of Fluids and Structures*, Vol. 48, 2014, pp. 27–45.
- [34] Willems, S., Gülhan, A., and Esser, B., "Shock induced fluid-structure interaction on a flexible wall in supersonic turbulent flow," *Progress in Flight Physics*, Vol. 5, 2013, pp. 285–308.
- [35] Hosters, N., Klaus, M., Schieffer, G., Behr, M., and Reimerdes, H.-G., "Towards aerothermoelastic simulations of supersonic flow through nozzles," *Progress in Propulsion Physics*, Vol. 4, 2013, pp. 637–654.
- [36] Brouwer, K. R., Gogulapati, A., and McNamara, J. J., "Interplay of Surface Deformation and Shock-Induced Separation in Shock/Boundary-Layer Interactions," AIAA Journal, 2017, pp. 1–16.
- [37] Pasquariello, V., "Analysis and Control of Shock-Wave Turbulent Boundary-Layer Interactions on Rigid and Flexible Walls," Ph.D. thesis, University Library of the Technical University of Munich, 2018.
- [38] Freydin, M., Dowell, E. H., Varigonda, S. V., and Narayanaswamy, V., "Response of a plate with piezoelectric elements to turbulent pressure fluctuation in supersonic flow," *Journal of Fluids and Structures*, Vol. 114, 2022, p. 103696.
- [39] Gao, M., Appel, D., Beck, A., and Munz, C.-D., "A high-order fluid-structure interaction framework with application to shock-wave/turbulent boundary-layer interaction over an elastic panel," *Journal of Fluids and Structures*, Vol. 121, 2023, p. 103950.
- [40] Daub, D., Willems, S., and Gülhan, A., "Experiments on aerothermoelastic fluid-structure interaction in hypersonic flow," *Journal of Sound and Vibration*, 2022, p. 116714.
- [41] Spottswood, S. M., Beberniss, T. J., Eason, T. G., Perez, R. A., Donbar, J. M., Ehrhardt, D. A., and Riley, Z. B., "Exploring the response of a thin, flexible panel to shock-turbulent boundary-layer interactions," *Journal of Sound and Vibration*, Vol. 443, 2019, pp. 74–89.
- [42] Thornton, E. A., "Thermal structures-four decades of progress," Journal of Aircraft, Vol. 29, No. 3, 1992, pp. 485–498.
- [43] Culler, A., and McNamara, J., "Fluid-thermal-structural modeling and analysis of hypersonic structures under combined loading," 52nd AIAA/ASME/ASCE/AHS/ASC Structures, Structural Dynamics and Materials Conference 19th AIAA/ASME/AHS Adaptive Structures Conference 13t, 2011, p. 1965.

- [44] Culler, A. J., and McNamara, J. J., "Studies on fluid-thermal-structural coupling for aerothermoelasticity in hypersonic flow," AIAA journal, Vol. 48, No. 8, 2010, pp. 1721–1738.
- [45] Culler, A. J., "Coupled fluid-thermal-structural modeling and analysis of hypersonic flight vehicle structures," Ph.D. thesis, The Ohio State University, 2010.
- [46] Purwar, A., Mahapatra, D. R., Thakor, N., Priyamvada, K., and Mukherjee, R., "A Methodology for Coupled Thermal-Structural Analysis and Structural Design of Scramjet Combustor," 30th International Symposium on Shock Waves 1, Springer, 2017, pp. 245–250.
- [47] Shahriar, A., and Shoele, K., "Nonlinear shock-induced flutter of a compliant panel using a fully coupled fluid-thermal-structure interaction model," *Journal of Fluids and Structures*, Vol. 124, 2024, p. 104047. https://doi.org/https://doi.org/10.1016/j.jfluidstructs.2023.104047, URL https://www.sciencedirect.com/science/article/pii/S0889974623002153.
- [48] Heil, M., Hazel, A. L., and Boyle, J., "Solvers for large-displacement fluid-structure interaction problems: segregated versus monolithic approaches," *Computational Mechanics*, Vol. 43, No. 1, 2008, pp. 91–101.
- [49] Lele, S. K., "Compact finite difference schemes with spectral-like resolution," *Journal of computational physics*, Vol. 103, No. 1, 1992, pp. 16–42.
- [50] Bhardwaj, R., Ziegler, K., Seo, J. H., Ramesh, K., and Nguyen, T. D., "A computational model of blast loading on the human eye," *Biomechanics and modeling in mechanobiology*, Vol. 13, No. 1, 2014, pp. 123–140.
- [51] Bhardwaj, R., and Mittal, R., "Benchmarking a coupled immersed-boundary-finite-element solver for large-scale flow-induced deformation," *AIAA journal*, Vol. 50, No. 7, 2012, pp. 1638–1642.
- [52] Gottlieb, S., and Shu, C.-W., "Total variation diminishing Runge-Kutta schemes," *Mathematics of computation*, Vol. 67, No. 221, 1998, pp. 73–85.
- [53] Cook, A. W., and Cabot, W. H., "Hyperviscosity for shock-turbulence interactions," *Journal of Computational Physics*, Vol. 203, No. 2, 2005, pp. 379–385.
- [54] Cook, A. W., and Cabot, W. H., "A high-wavenumber viscosity for high-resolution numerical methods," *Journal of Computational Physics*, Vol. 195, No. 2, 2004, pp. 594–601.
- [55] Fiorina, B., and Lele, S. K., "An artificial nonlinear diffusivity method for supersonic reacting flows with shocks," *Journal of Computational Physics*, Vol. 222, No. 1, 2007, pp. 246–264.
- [56] Kawai, S., and Lele, S. K., "Localized artificial viscosity and diffusivity scheme for capturing discontinuities on curvilinear and anisotropic meshes," Center for Turbulence Research Annual Research Briefs, 2007.
- [57] Aubry, S., Foulk, J. W., Jones, R. E., Kimmer, C. J., Klein, P. A., Marin, E. B., Regueiro, R. A., Zeigler, D. A., and Zimmerman, J. A., "TAHOE Ver 1.0, Version 00,", 10 2002. URL https://www.osti.gov/biblio/1230555.
- [58] Hilber, H. M., Hughes, T. J., and Taylor, R. L., "Improved numerical dissipation for time integration algorithms in structural dynamics," *Earthquake Engineering & Structural Dynamics*, Vol. 5, No. 3, 1977, pp. 283–292.
- [59] Bernardini, M., Modesti, D., Salvadore, F., and Pirozzoli, S., "STREAmS: a high-fidelity accelerated solver for direct numerical simulation of compressible turbulent flows," *Computer Physics Communications*, Vol. 263, 2021, p. 107906.
- [60] Bodony, D. J., "Analysis of sponge zones for computational fluid mechanics," *Journal of Computational Physics*, Vol. 212, No. 2, 2006, pp. 681–702.
- [61] Mani, A., "On the reflectivity of sponge zones in compressible flow simulations," *Center for Turbulence Research, Annual Research Briefs*, 2010, pp. 117–133.
- [62] Seo, J. H., and Mittal, R., "A high-order immersed boundary method for acoustic wave scattering and low-Mach number flow-induced sound in complex geometries," *Journal of computational physics*, Vol. 230, No. 4, 2011, pp. 1000–1019.
- [63] Volpiani, P. S., Bernardini, M., and Larsson, J., "Effects of a nonadiabatic wall on supersonic shock/boundary-layer interactions," *Physical Review Fluids*, Vol. 3, No. 8, 2018, p. 083401.